Journal of ELECTRONIC MATERIALS, Vol. 45, No. 8, 2016
DOI: 10.1007/s11664-016-4595-1

Dielectric Properties of $SrMnO_3$-doped $K_{0.5}Na_{0.5}NbO_3$ Lead-Free Ceramics

JIANMING DENG,[1] XIAOJUN SUN,[1] LAIJUN LIU,[1,3] SAISAI LIU,[1] YANMIN HUANG,[1] LIANG FANG,[1] and BRAHIM ELOUADI[2]

1.—Guangxi Universities Key Laboratory of Non-ferrous Metal Oxide Electronic Functional Materials and Devices, Key Laboratory of Nonferrous Materials and New Processing Technology, Ministry of Education, College of Materials Science and Engineering, Guilin University of Technology, Guilin 541004, People's Republic of China. 2.—Laboratory of Chemical Analysis Elaboration and Materials, Engineering (LEACIM), Université de La Rochelle, Avenue Michel Crépeau, 17042 La Rochelle Cedex 01, France. 3.—e-mail: ljliu2@163.com

$(1-x)K_{0.5}Na_{0.5}NbO_3$-$xSrMnO_3$ $(0.02 \le x \le 0.08)$ (KNN-xSM) ceramics were fabricated by a conventional solid-state technique. X-ray diffraction of the samples revealed that the crystal structure changes from orthorhombic to tetragonal, and finally to pseudocubic symmetry with increasing x. Temperature dependence of dielectric properties showed that the temperature (T_m) corresponding to the maximum of dielectric permittivity decreased with increasing x. Two dielectric relaxation processes occurred at high temperatures, which were attributed to grain and grain boundary responses, respectively. Polarization hysteresis loops (P-E) at different electrical fields were displayed. $P_{r\max}$ degenerated with the increase of SM due to the thermally activated leakage current increases. The relationship between electrical properties and defect compensation mechanism is discussed.

Key words: Ceramics, electronic materials, electrochemical techniques, defect, dielectric properties

INTRODUCTION

In recent years, alkaline niobates, such as $K_xNa_{1-x}NbO_3$ based ceramics, have attracted much attention for fundamental research and technological applications, especially for $K_{0.5}Na_{0.5}NbO_3$ (KNN) ceramics, due to their superior performance in piezoelectric and ferroelectric applications.[1] It could be considered as a promising candidate for the miniaturization of electronic devices such as sensors and resonators. Since the strong toxicity and high evaporation of lead oxide have caused a crucial environmental pollution, it is worthy to develop lead-free piezoelectric ceramics with good piezoelectric properties and to be environmentally friendly for replacing the lead-containing ceramics in various applications.[2,3]

(Received November 20, 2015; accepted April 28, 2016; published online May 10, 2016)

However, it is very difficult to obtain dense and well-sintered KNN ceramics. Only 90.0% theoretical density of the ceramics was achieved by using an ordinary sintering process, because of the volatility of alkaline elements at high temperatures, which leads to poor dielectric, ferroelectric, and piezoelectric properties. Although the KNN ceramics prepared by the hot-pressing technique showed good piezoelectric properties and high density,[4] the cost of this method is very expensive. Therefore, many researchers focus on improve the density and electrical properties of KNN-based ceramics by introducing new compositions or dopants/additives.[5–14] It is reported by Kosec et al.[15] that Sr doped into KNN showed dielectric relaxation behavior. Lin et al.[16] found that MnO_2-doped into KNN crystals gave rise to enhanced piezoelectric coefficient d_{33} and dielectric permittivity ε_r, whereas there was decreased dielectric loss. However, the study of electrical properties of Sr and Mn co-doped KNN are not clear. On the other hand, heterovalent ions

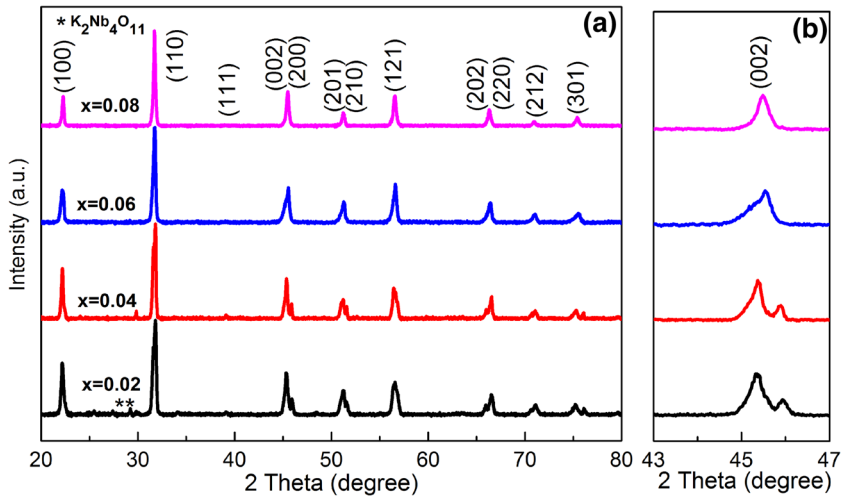

Fig. 1. XRD patterns of KNN-*x*SM ceramics with $x = 0.02$, 0.04, 0.06, and 0.08. (a) 2θ from 20° to 80° and (b) 2θ from 43° to 47°.

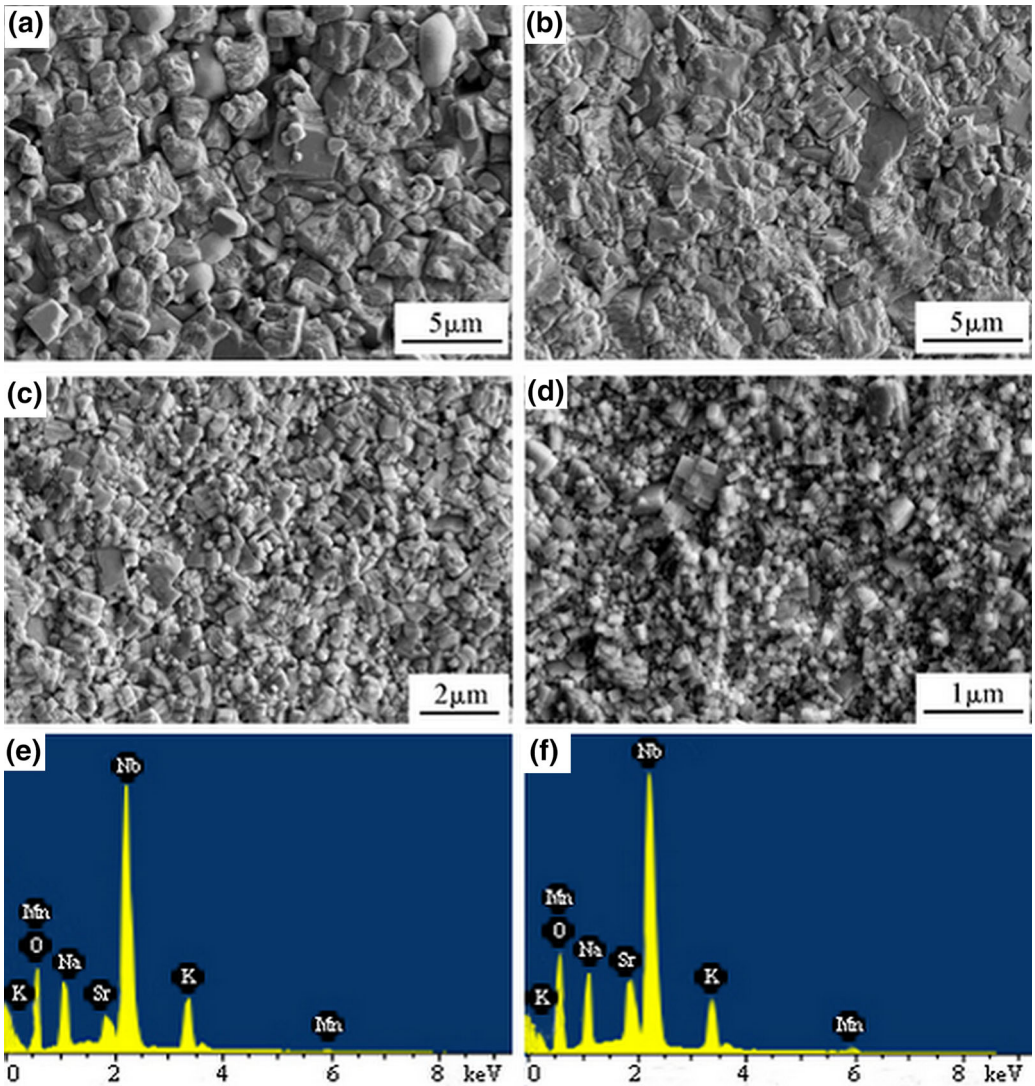

Fig. 2. SEM micrographs of KNN-*x*SM ceramics with (a) $x = 0.02$, (b) $x = 0.04$, (c) $x = 0.06$, and (d) $x = 0.08$. EDS spectra of KNN-*x*SM ceramics with (e) $x = 0.06$ and (f) $x = 0.08$.

substitution could result in the creation and combination of point defects based on a defect compensation mechanism. Point defects, such as oxygen vacancy, often worsen high dielectric properties due to the mobility of defects. Therefore, charge carriers transportation at high temperature should be focused on in heterovalent ion doped KNN.

In this work, the structure, dielectric properties, and impedance spectroscopy of $(1-x)K_{0.5}Na_{0.5}NbO_3$-$xSrMnO_3$ ceramics were investigated. The phase transition changes from tetragonal to cubic with the increase of x. Two dielectric relaxation processes are present above T_m, which associates with grain and grain boundary responses, respectively.

EXPERIMENTAL

$(1-x)K_{0.5}Na_{0.5}NbO_3$-$xSrMnO_3$ (x = 0.02, 0.04, 0.06, and 0.08) [abbr. to KNN-xSM] ceramics were prepared by solid-state reactions. All of the reagents used in the experiments are of analytic grade. Stoichiometric amounts of purity Na_2CO_3 (99.8%), K_2CO_3 (99%), $SrCO_3$ (99.98%), Nb_2O_5 (99.99%) and MnO_2 (97.5%) were weighted and mixed by ball milling in alcohol for 8 h using zirconia balls. After drying, the mixed powders were ground and then calcined in air at 900°C for 4 h using heating rates of 5°C/min. The calcined powder was ball-milled and dried again to obtain homogeneous powder. Pellets 12 mm in diameter and about 1.10 mm in thickness were uniaxially pressed at 350 MPa using a 5% PVA binder. Slow heating at 550°C for 2 h burned out the binder. Finally, the pellets were sintered in air at 1100°C for 4 h using heating rates of 5°C/min to obtain a compact ceramic bulk. All samples were cooled in a furnace.

Crystal structure and microstructure of the samples were identified by x-ray diffraction (XRD, PANalytical X'Pert PRO) using Cu $K\alpha$ radiation (λ = 1.5406 Å) in the range of 2θ = 20°–80° and scanning electron microscopy (SEM, JSM-6380, Japan) measurements, respectively. Silver paste electrodes were formed at the two surfaces of the samples and fired at 650°C for 30 min. The dependence of the dielectric permittivity on temperature was measured with a precision impedance analyzer (Agilent 4294A, USA) over the frequency range 40 Hz to 1 MHz with applied voltage of 500 mV at a

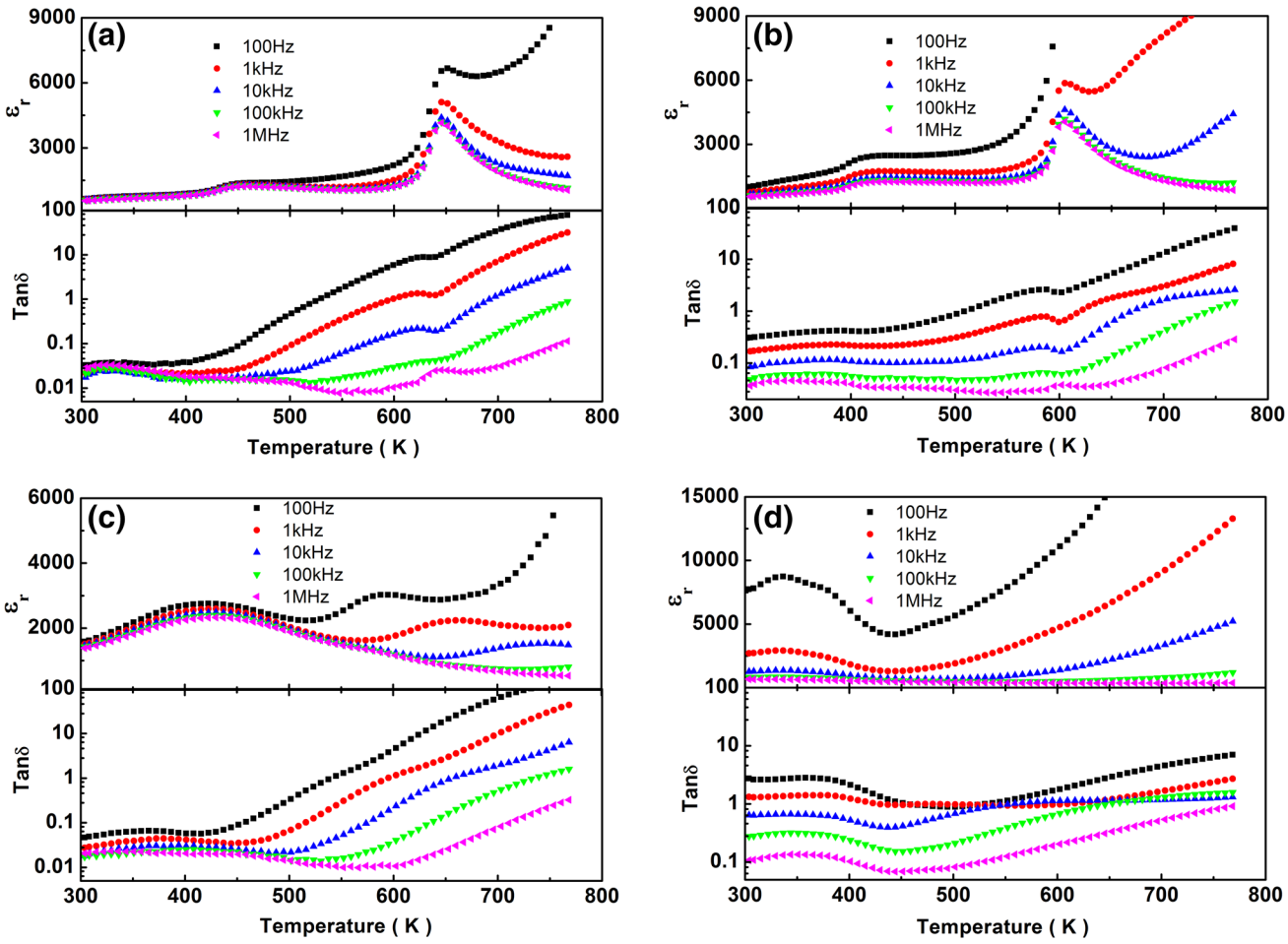

Fig. 3. Temperature dependence of dielectric permittivity and dielectric loss factor of the KNN-xSM ceramics in the frequency range of 100 Hz to 1 MHz. (a) x = 0.02, (b) x = 0.04, (c) x = 0.06, and (d) x = 0.08.

temperature range of 300 K to 800 K. The ferroelectric hysteresis loops were measured under different electrical fields at room temperature using a ferroelectric tester (TF ANALYZER 2000) at 1 Hz.

RESULTS AND DISCUSSION

XRD patterns of the KNN-xSM ceramics at room temperature are shown in Fig. 1. It can be seen from Fig. 1a that the main phase agrees with the pure KNN [ICDD PDF card no. 01-077-0038]. The XRD patterns show a pure perovskite structure with $x \geq 0.06$, whereas a small amount of secondary phase $K_2Nb_4O_{11}$ was detected for $x < 0.06$. It suggests that MnO_2 is a good sintering aid for restraining the secondary phase. Figure 1b shows the enlarged XRD patterns of the samples in the 2θ range 43°–47°. With increasing x value, the reflects of (002) and (200) near $2\theta \sim 45°$, gradually merge into a single peak. This suggests that the crystalline structure of the compositions varies from a tetragonal phase to a rhombohedral phase. It indicates that the KNN-xSM ceramics undergoes a tetragonal–orthorhombic transition near $x = 0.06$ and a cubic-tetragonal transition near $x = 0.08$. The phase evolution could be proved by dielectric measurements.

Figure 2a–d reveal the scanning electron micrograph of KNN-xSM ceramics. It is clear that the average grain size of the samples decreased with the increase of SM content. All the samples consist of submicron-sized grains with a small number of pores that have dimensions comparable to the grains. Characteristic quasi-cubic grains appear in the all samples. The samples have an inhomogeneous microstructure with bimodal grain size distribution. The sintering of alkaline niobate-based piezoelectric ceramics is usually performed at temperatures near the melting points. As a result, abnormal grain growth often appears. On the other hand, some oxides with low melting points can lower the sintering temperature effectively and restrain abnormal grain growth, which is the case with the addition of MnO_2. Figure 2e and f shows the EDS spectra of the samples for $x = 0.06$ and 0.08, Sr and Mn can be detected in these ceramics.

Figure 3 shows the sintering temperature dependence of dielectric permittivity (ε_r) and dielectric loss ($\tan\delta$) of the KNN-xSM ceramics in the frequency range of 100 Hz to 1 MHz. In Fig. 3a and b, there were two dielectric peaks in the temperature dependence of dielectric permittivity that correspond to orthorhombic-tetragonal phase transition (at low temperature) and tetragonal-cubic phase

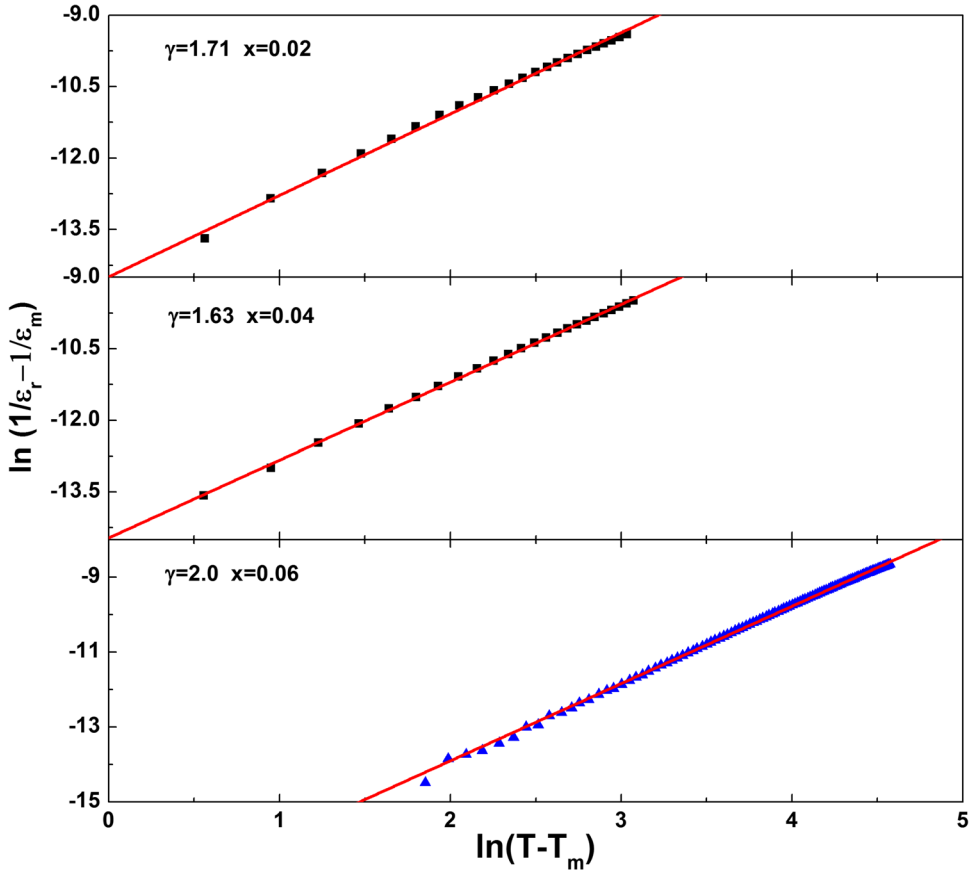

Fig. 4. The plots of $\ln(1/\varepsilon_r - 1/\varepsilon_m)$ as a function of $\ln(T - T_m)$ at 1 MHz for the KNN-xSM ceramics.

transition (at high temperature). With increasing SM concentration, both phase transition temperatures shift toward lower temperature. Only one phase transition peak can be found above room temperature in the samples of $x = 0.06$ and 0.08. Furthermore, the peak becomes very diffuse. The dielectric permittivity at room temperature increases rapidly with increasing SM concentration at 1 kHz, ε_r is 620, 756, 1508, and 2702 for the samples of $x = 0.02$, 0.04, 0.06, and 0.08, respectively. The temperature dependence of dielectric loss factor remains unchanged below 450 K but increases rapidly at high temperatures. It is noted that a thermal activated dielectric relaxation occurs in the sample of $x = 0.06$. The dielectric peak above T_m shifts to higher temperatures with the increasing of the measuring frequency.

The dielectric permittivity of a normal ferroelectric should obey the Curie–Weiss law. For the relaxor ferroelectrics, the reciprocal of the dielectric permittivity and temperature obey the Uchino and Nomura function, a modified Curie–Weiss law.[17]

$$\frac{1}{\varepsilon} - \frac{1}{\varepsilon_m} = \frac{(T - T_m)^\gamma}{C}, \quad (1)$$

where C is the Curie constant and γ is called a diffusion coefficient ranging between 1 (a normal ferroelectric) and 2 (an ideal relaxor ferroelectric).[18] Figure 4 shows the plots of $\ln(1/\varepsilon_r - 1/\varepsilon_m)$ as a function of $\ln(T - T_m)$ at 1 MHz for the KNN-xSM ceramics. All the samples exhibit a linear relationship. The slope of the fitting curves are used to determine the γ value. The values of γ varies from 1.71 to 2.0. It indicates that the ceramics have transformed gradually from diffuse-phase ferroelectrics to relaxor ferroelectrics with the increasing of x.

Figure 5 shows impedance complex plane plots of the KNN-xSM ceramics at different temperatures. The resistances of the ceramics decrease with an increase of temperature, indicating that the ceramics have negative temperature coefficients. The features of the impedance spectra are almost similar at different temperatures for each sample. However,

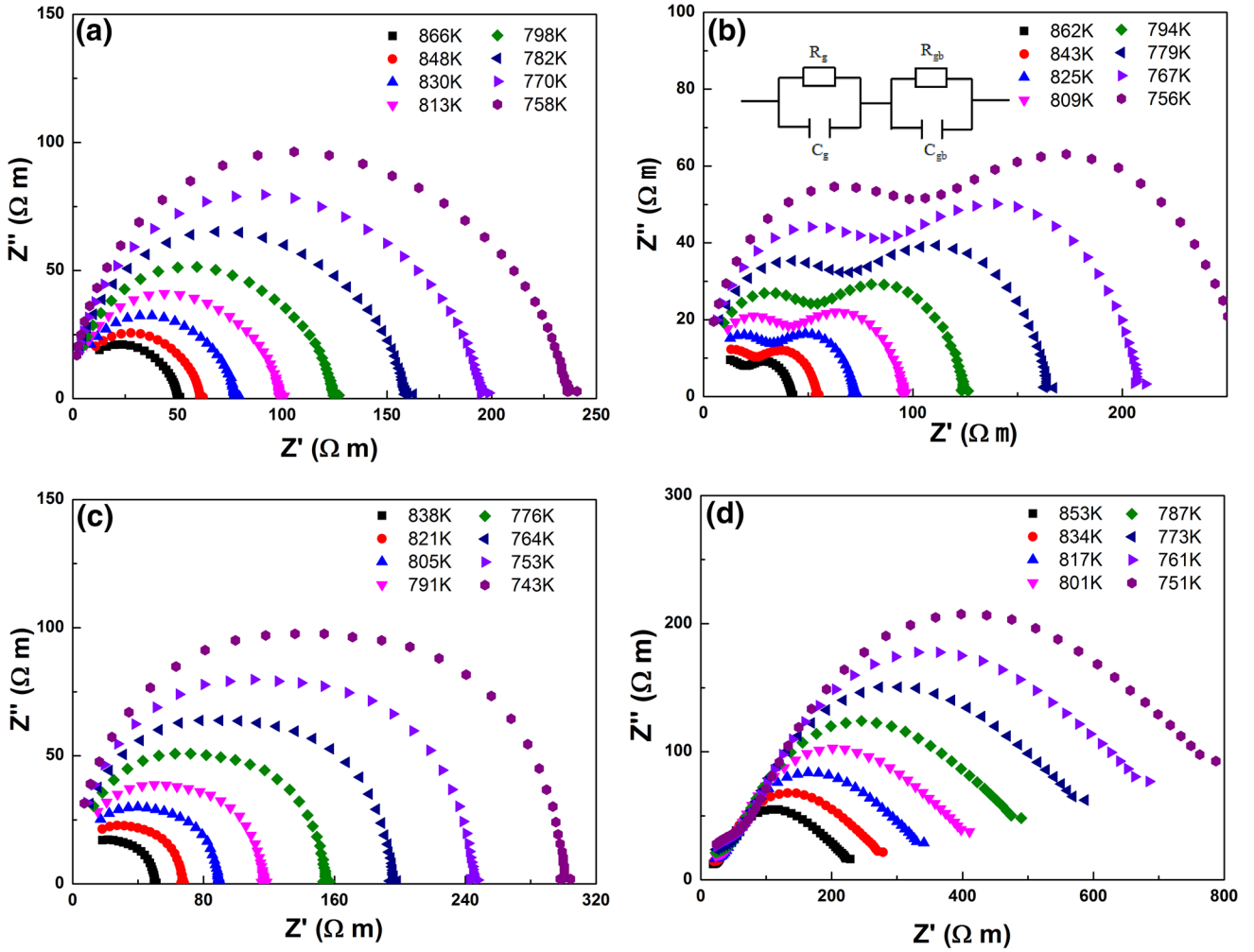

Fig. 5. Complex impedance plots of the KNN-xSM ceramics at different temperatures. (a) $x = 0.02$, (b) $x = 0.04$, (c) $x = 0.06$, and (d) $x = 0.08$.

the decreases in radius of curvature of the arcs with increasing temperature reveals the increase of conductivity of the samples. As shown in Fig. 5a and c, only one semicircle arc can be observed at different temperatures. The semicircle arcs should arise from the grain boundary effect.[14] The grain boundary resistance (R_{gb}) could be obtained directly from the intercept on the Z'-axis. The semicircle radius decreases with the increase of temperature, which suggests the decrease of the grain boundary resistance. As shown in Fig. 5b and d, each complex impedance plot shows two semicircles. There are two dielectric relaxations, corresponding to grain and grain boundaries, respectively. The small arc is associated with grain response in the high frequency range, the other is related to a grain boundary response at low-frequency regions. These two semicircular arcs can be modeled as an equivalent circuit consisting of two parallel RC elements connected in series: one RC element, i.e., R_gC_g, represents the semiconducting grains, and the other, i.e., $R_{gb}C_{gb}$, represents the insulating grain boundary regions, as shown in the inset of Fig. 5b. For such an equivalent circuit, each RC element ideally arises in a semicircular arc in the complex impedance plane Z^*[19] described as follows:

$$Z^* = Z' - iZ'' \tag{2}$$

In AC circuits, for a pure resistor and capacitor, $Z^* = R$ and $1/i\omega C$, respectively. Therefore, the impedance can be expressed as Eq. 3 for each RC element.

$$Z^* = \frac{1}{1/R + i\omega C} = \frac{R}{1 + i\omega RC} \tag{3}$$

In our experiment, the impedance spectrum can be modeled as two RC elements connected in series. Therefore, the complex impedance ($Z^* = Z' - iZ''$) here can be expressed as[20]

$$Z' = \frac{R_g}{1 + (\omega R_g C_g)^2} + \frac{R_{gb}}{1 + (\omega R_{gb} C_{gb})^2} \tag{4}$$

and

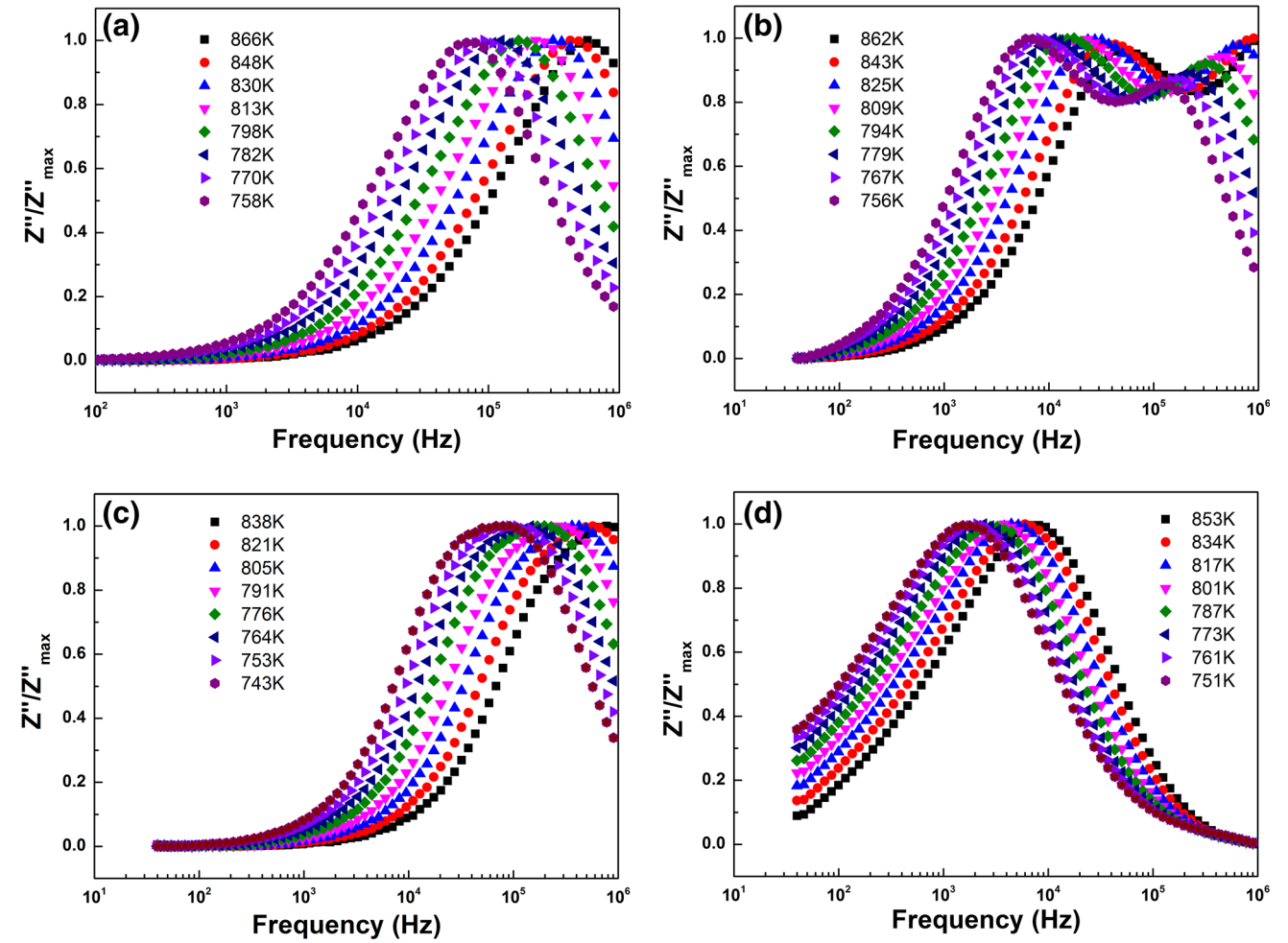

Fig. 6. Normalized imaginary parts Z''/Z''_{max} of impedance as a function of frequency for KNN-xSM ceramics at different temperatures. (a) $x = 0.02$, (b) $x = 0.04$, (c) $x = 0.06$, and (d) $x = 0.08$.

$$Z'' = R_g\left[\frac{\omega R_g C_g}{1+(\omega R_g C_g)^2}\right] + R_{gb}\left[\frac{\omega R_{gb} C_{gb}}{1+(\omega R_{gb} C_{gb})^2}\right], \quad (5)$$

where R and C are the resistance and capacitance, respectively, the subscripts g and gb refer to the grains and grain boundaries, respectively, and ω is the angular frequency. Based on Eq. 5, the response peaks of the grains and the grain boundaries are located at $1/(2\pi R_g C_g)$ and $1/(2\pi R_{gb} C_{gb})$, respectively, and the peak value is proportional to the associated resistance.[21,22] The above results demonstrate that the samples of x = 0.04 and x = 0.08 are electrically heterogeneous, which is well consistent with the internal barrier layer capacitance (IBLC) model.[23–25]

The normalized imaginary parts Z''/Z''_{max} of impedance as a function of frequency in KNN-xSM ceramics at different temperatures are shown in Fig. 6. The Z''/Z''_{max} shifts to teh higher frequency side with increasing temperature. Furthermore, the Z''/Z''_{max} values for all temperatures also merge together for $x < 0.08$ below 1 kHz and x = 0.08 above 100 kHz. It suggests that the relaxation behavior is related tothe thermal activation process.[26] According to Fig. 6b and c, the grain response shifts to lower frequency with the increases of SM concentration. The two responses are combined in the sample of x = 0.08. For the sample of x = 0.02, the grain response could be out of our measuring frequency window. A possibility is that the SM gradually enters the grain from grain boundary to form a homogeneous composition between grain and grain boundary. The relationship between temperature and relaxation frequency in Fig. 6 obeys the Arrhenius relation given by

$$\omega_{max} = \omega_0 \exp\left[-\frac{E_{rel}}{k_B T}\right], \quad (6)$$

where ω is the angle frequency, ω_0 is the pre-exponential factor and k_B is the Boltzmann constant, $k_B = 8.617 \times 10^{-5}$ eV/K, T is the Kelvin temperature, and E_{rel} is the activation energy for the dielectric relaxation. The relationship between

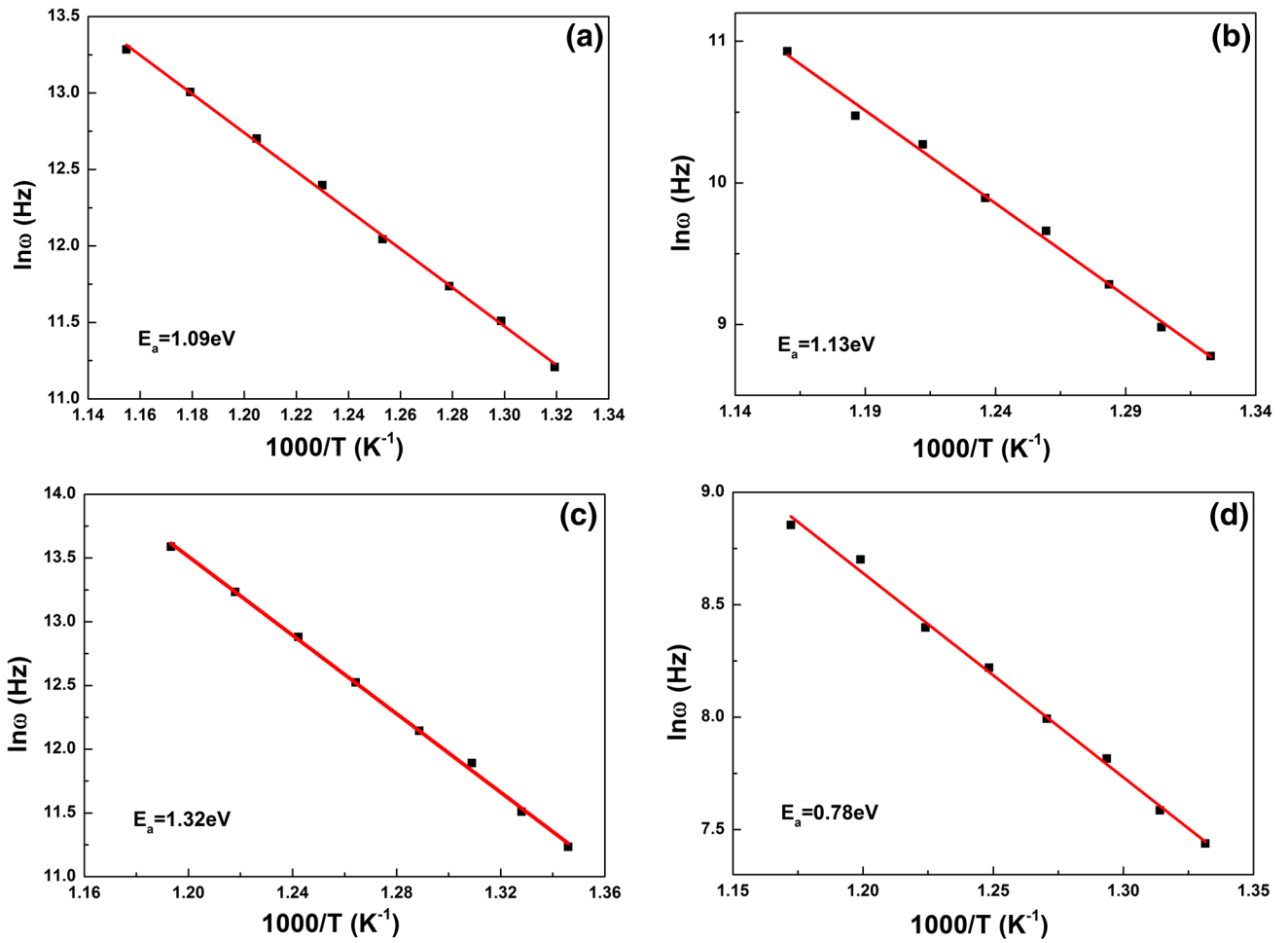

Fig. 7. Temperature dependence of the relaxation frequency obtained from the normalized imaginary part of impedance plots for the KNN-xSM ceramics. (a) x = 0.02, (b) x = 0.04, (c) x = 0.06 and (d) x = 0.08.

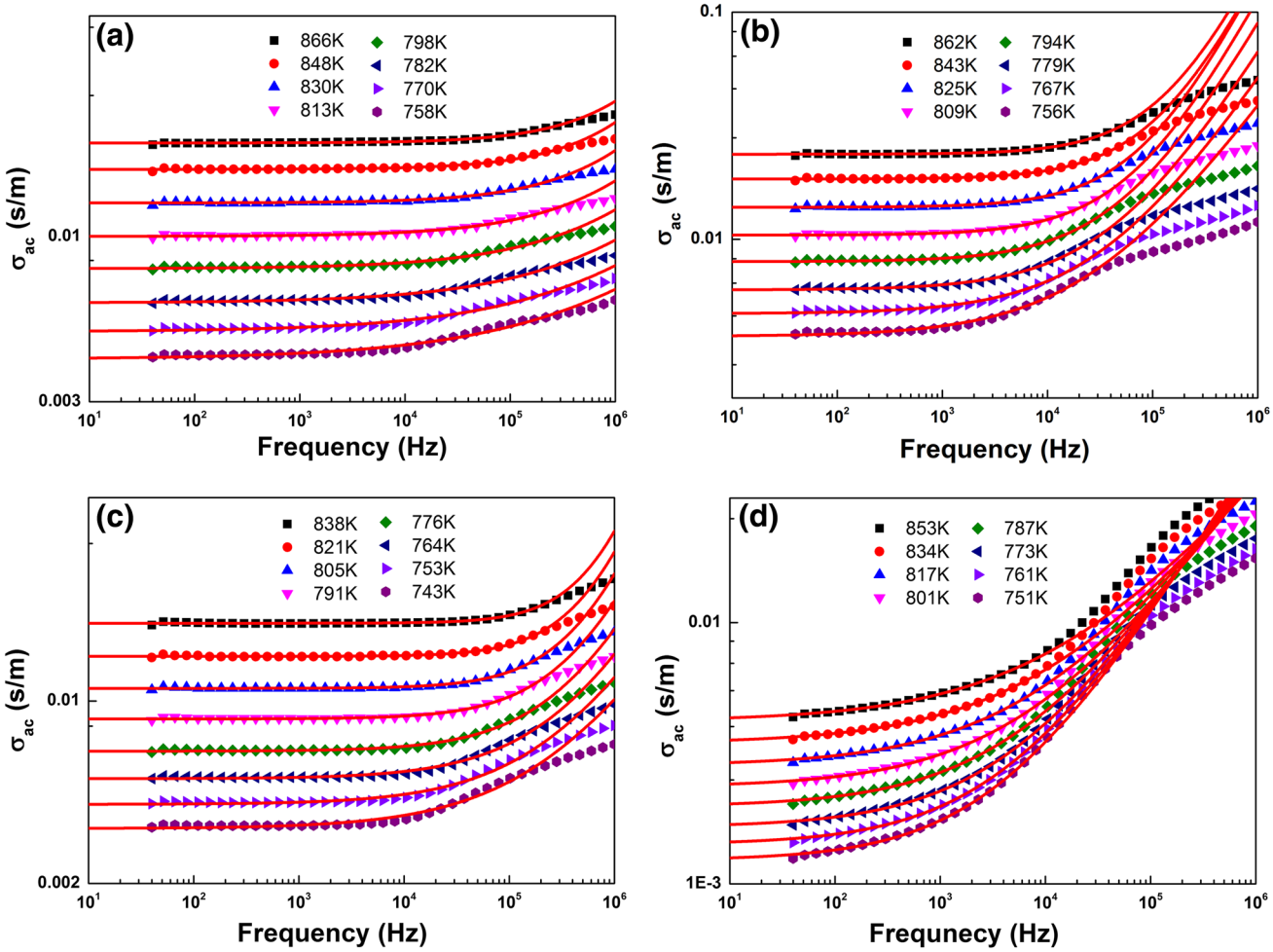

Fig. 8. Frequency dependence of the real part of ac conductivity of KNN-*x*SM ceramics at different temperatures. (a) $x = 0.02$, (b) $x = 0.04$, (c) $x = 0.06$, and (d) $x = 0.08$.

frequency and reciprocal temperature was fitted and shown in Fig. 7. According to the slopes of the fitted straight lines, the value of activation energy of KNN-*x*SM ceramics with $x = 0.02$, 0.04, 0.06, and 0.08 is 1.09 eV, 1.13 eV, 1.32 eV, and 0.78 eV, respectively. The activation energy increases firstly and then decreases with increasing SM concentration. The activation energy of oxygen vacancy has been reported to be in the range 0.3 eV to 0.5 eV for single-ionized oxygen vacancies and 0.6 eV to 1.2 eV for doubly-ionized oxygen vacancies.[27–33] Therefore, the activation energy of a grain boundary should be attributed to the doubly-ionized oxygen vacancy.

Figure 8 displays the real part of *ac* conductivity (σ_{dc}) at different temperatures for KNN-*x*SM ceramics. The *ac* conductivity plots as a function of frequency shows two conduction processes at different temperatures. The curves exhibit a step-like characteristic due to the grain boundary effect where a corresponding relaxation peak is observed in Fig. 6. The σ_{ac} almost saturates to a constant value at low frequencies, which is approximately equal to the dc conductivity σ_{dc}. As the frequency f is increased to 10 kHz, σ_{ac} also increases as a result of grain boundary relaxation. It could be described by the so-called "universal dielectric response" law[34]:

$$\sigma'(\mathrm{f}) = \sigma_{dc} + \sigma_0 f^s, \qquad (7)$$

where σ_{dc} is the dc bulk conductivity, f is the frequency, σ_{dc} is a constant, and $0 \le s \le 1$. Equation 7 describes the relationship between typical thermally-assisted tunneling and localized states. This law describes one phenomenon that is associated with many body interactions between charges and dipoles.[35] The σ_{dc} at different temperatures can be obtained according to a nonlinear fitting based on Eq. 7, which is shown in Fig. 9. Moreover, it is suggested that the value of dielectric permittivity contributed by the universal relaxation process is much less than the thermally activated space charges at high temperatures.

The temperature dependence of σ_{dc} thus obtained follows the Arrhenius law given by:

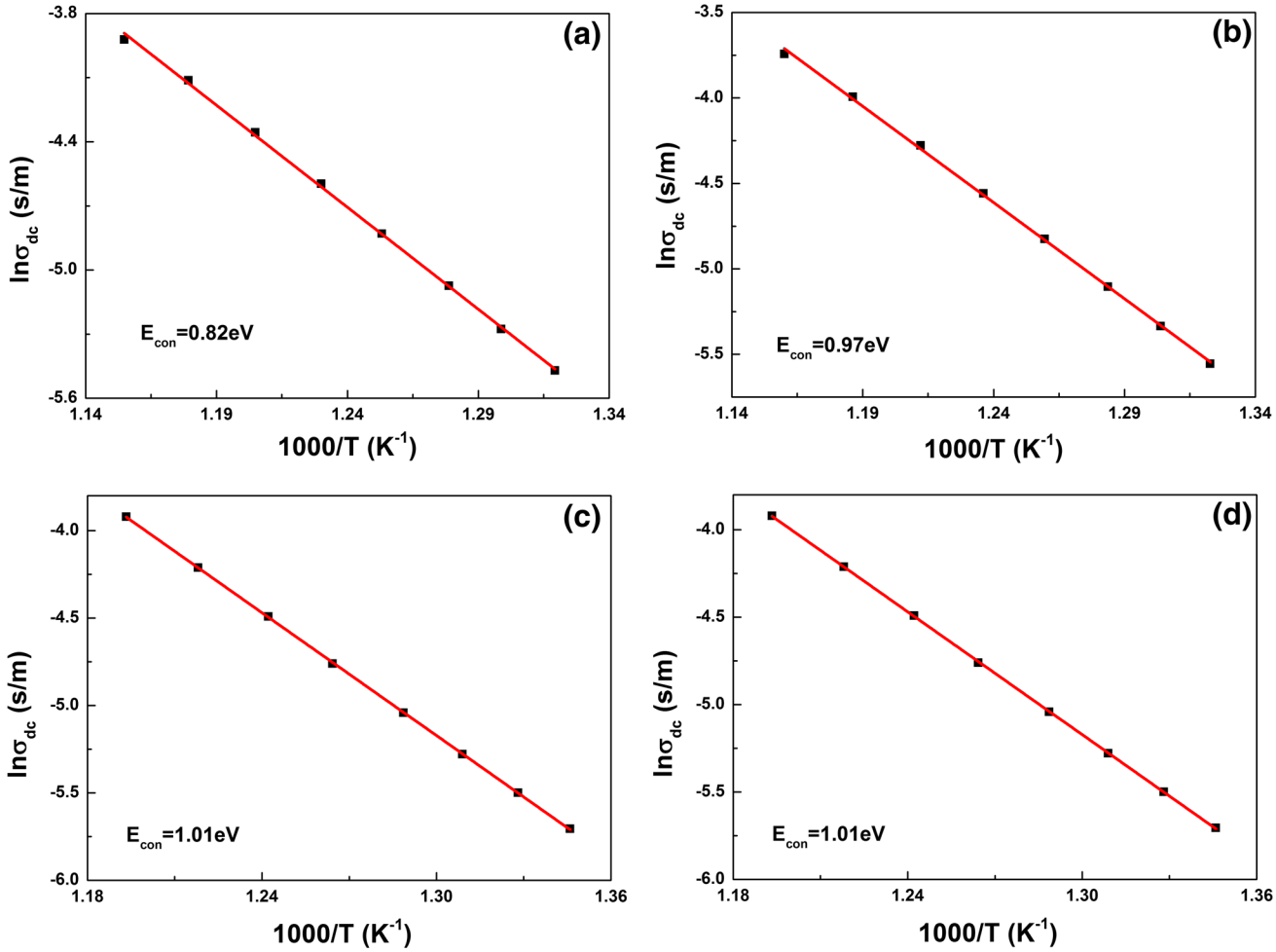

Fig. 9. Arrhenius plots of the dc conductivity of the KNN-*x*SM ceramics. (a) x = 0.02, (b) x = 0.04, (c) x = 0.06, and (d) x = 0.08.

$$\sigma_{dc} = T^{-1}\sigma_0 \exp\left(-\frac{E_{con}}{k_B T}\right). \quad (8)$$

The activation energy for conduction (E_{con}) of KNN-*x*SM ceramics with x = 0.02, 0.04, 0.06, and 0.08 is 0.82 eV, 0.97 eV, 1.01 eV, and 0.71 eV, respectively, from the slope of the straight line obtained from $\ln\sigma_{dc} \sim 1000/T$ plot in Fig. 9. With the increasing SM concentration, the activation energy for conduction first increases and then decreases, which agrees with relaxation activation energy.

It is well known that the evaporation of Na/K occurs during sintering and results in oxygen vacancies that can be written as Eqs. 9 and 10[36]:

$$Na_{Na} \rightarrow Na + V'_{Na} + 1/2V_0^{\cdot\cdot}, \quad (9)$$

$$K_K \rightarrow K + V'_K + 1/2V_0^{\cdot\cdot}, \quad (10)$$

$$Mn'_{Nb} + 1/2V_0^{\cdot\cdot} \rightarrow Mn_{Nb}, \quad (11)$$

$$V_0^{\cdot} \rightarrow V_0^{\cdot\cdot} + e'. \quad (12)$$

The concentration of the sodium/potassium vacancies, V'_{Na} or V'_K, would be double that of one or two oxygen vacancy (ies), $V_0^{\cdot\cdot}/V_0^{\cdot}$.[37] The oxide of manganese could decrease the concentration of the oxygen vacancy according to Eq. 11. With the increasing of the SM, it diffuses into the grain from grain boundary. The concentration of oxygen vacancy decreases with the entrance of the SM in grains. Therefore, the activation energy increases. With further increase of the SM to x = 0.08, grains and grain boundaries have the same/homogeneous composition, and the single-ionized oxygen vacancy can be presented in Eq. 12. Therefore, the activation energy becomes smaller.

Figure 10 shows the room temperature polarization versus the electric field (*P-E*) hysteresis loops of the KNN-*x*SM ceramics with x = 0.02, 0.04, 0.06, and 0.08 measured at 1 Hz. It can be seen that both coercive the electric field and the remanent polarization gradually tend to "saturated" with increasing voltages. Furthermore, the absence of clear hysteresis behavior for lower x contents can be related to a decreased T_m, as shown in Fig. 3.[38]

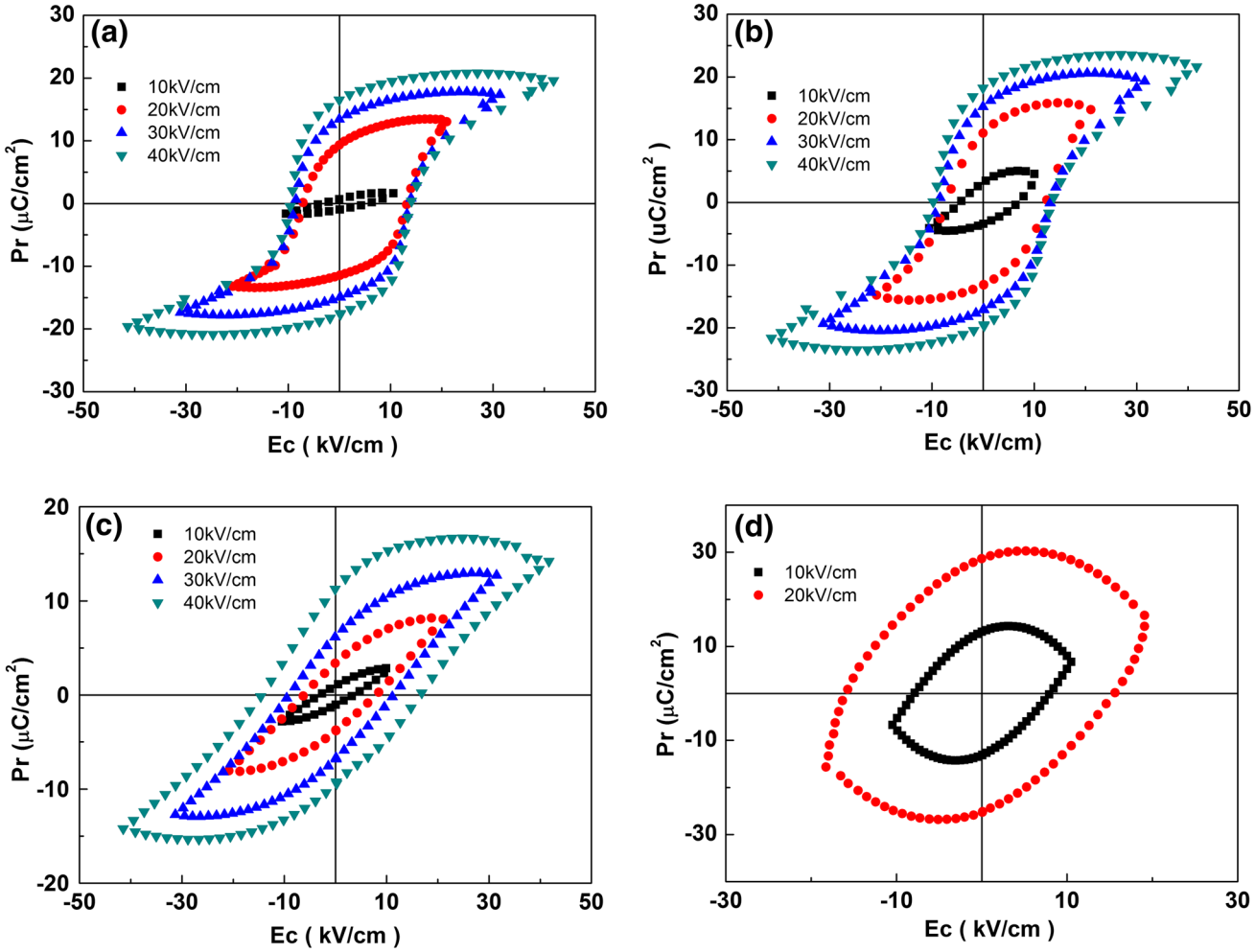

Fig. 10. The hysteresis loop of the KNN-*x*SM ceramics at different voltages. (a) $x = 0.02$, (b) $x = 0.04$, (c) $x = 0.06$, and (d) $x = 0.08$.

When the voltage rises to 40 kV/cm, all of the ceramics exhibit well saturated hysteresis loops except the sample of $x = 0.16$. For the sample with $x = 0.04$, the remanent polarization (P_r) increases to the highest value of 20 $\mu C/cm^2$. For $x = 0.16$, the hysteresis loops show a rounded shape due to large leakage currents, which agrees well with the results of temperature dependence analysis.

CONCLUSIONS

The dielectric, ferroelectric, and impedance behavior of KNN-*x*SM ceramics were analyzed according to a defect compensation mechanism. The ceramics with $x = 0.04$ exhibit good ferroelectric properties with remanent polarization (P_r) $\sim$ 20 $\mu C/cm^2$. In addition, the complex impedance analysis indicates that the samples of $x = 0.04$ and $x = 0.08$ were electrically heterogeneous, consisting of insulating grain boundaries and semiconducting grains, which was well consistent with the internal barrier layer capacitance (IBLC) model. The difference of activation energy indicates variable concentration of oxygen vacancy in grains and grain boundaries.

ACKNOWLEDGEMENTS

This work was financially supported by the Natural Science Foundation of China (Grant Nos. 51002036, 11264010, 21061004 and 50962004), and by the Natural Science Foundation of Guangxi (Grant Nos. BA053007, FA139003).

REFERENCES

1. G.H. Haertling, *J. Am. Ceram. Soc.* 82, 797 (1999).
2. D.M. Lin, Q.J. Zheng, and K.W. Kwok, *J. Mater. Sci.: Mater. Electron.* 21, 649 (2010).
3. Y. Saito, H. Takao, and T. Tani, *Nature* 84, 432 (2004).
4. R.E. Jaeger and L. Egerton, *J. Am. Ceram. Soc.* 45, 209 (1962).
5. K. Kakimoto, I. Masuda, and H. Ohsato, *Jpn. J. Appl. Phys.* 42, 6102 (2003).
6. M. Kosec and D. Kolar, *Mat. Res. Bull.* 10, 335 (1975).
7. B. Malic, J. Bernard, J. Holc, D. Jenko, and M. Kosec, *J. Eur. Ceram. Soc.* 25, 2707 (2005).
8. S. Liang and J. Zhu, *Ceram. Int.* 40, 2763 (2014).
9. L.H. Zhang, S.L. Wang, and F.H. Liu, *J. Electron. Mater.* 44, 1 (2015).

10. L.B. Fei, D.P. Shi, Y.M. Huang, and L.J. Liu, *J. Mater. Sci.: Mater. Electron.* 26, 7159 (2015).
11. X. Vendrell and J.E. García, *J. Eur. Ceram. Soc.* 35, 125 (2015).
12. C. Kiang, I. Tan, and K. Yao, *Ceram. Int.* 38, 2513 (2012).
13. S.S. Wu, W.F. Zhu, L.J. Liu, D.P. Shi, S.Y. Zheng, Y.M. Huang, and L. Fang, *J. Electron. Mater.* 43, 1055 (2014).
14. W. Wu and D. Xiao, *J. Alloy Compd.* 509, L284 (2011).
15. M. Kosec, V. Bobnar, and M. Hrovat, *J. Mater. Res.* 19, 1849 (2004).
16. D.B. Lin, Z.R. Li, and S.J. Zhang, *J. Am. Ceram. Soc.* 93, 941 (2010).
17. G.P. Arlt and N.A. Ertsev, *J. Appl. Phys.* 70, 2283 (1991).
18. K. Uchino and S. Nomura, *Ferroelectrics* 44, 55 (1982).
19. D.C. Sinclair, T.B. Adams, F.D. Morrison, and A.R. West, *Appl. Phys. Lett.* 80, 2153 (2002).
20. Y.Y. Li, P.F. Liang, X.L. Chao, and Z.P. Yang, *Ceram. Int.* 39, 7879 (2013).
21. Y. Zhao, P.F. Liang, L.H. Yang, P.G. Shi, X.L. Chao, and Z.P. Yang, *J. Mater. Sci.: Mater. Electron.* 26, 1959 (2015).
22. J.M. Deng, X.J. Sun, S.S. Liu, L.J. Liu, T.X. Yan, L. Fang, and B. Elouadi, *J. Adv. Dielectr.* 6, 1650009 (2016).
23. J. Li, A.W. Sleight, and M.A. Subramanian, *Solid State Commun.* 135, 260 (2005).
24. Z.P. Yang, L.J. Zhang, X.L. Chao, L.R. Xiong, and J. Liu, *J. Alloy Compd.* 509, 8716 (2011).
25. H.M. Ren, P.F. Liang, and Z.P. Yang, *Mater. Res. Bull.* 45, 1608 (2010).
26. L.J. Liu, Y.M. Huang, Y.H. Li, M.X. Wu, L. Fang, C.Z. Hu, and Y.Z. Wang, *Phys. B* 407, 136 (2012).
27. K. Uchino and S. Nomura, *Ferroelectrics Lett. Sect.* 44, 55 (1982).
28. L.J. Liu, Y.M. Huang, C.X. Su, L. Fang, M.X. Wu, C.Z. Hu, and H.Q. Fan, *Appl. Phys. A* 104, 1047 (2011).
29. C. Verdier, F.D. Morrison, and D.C. Lupascu, *J. Appl. Phys.* 97, 024107 (2005).
30. H.I. Yoo, C.R. Song, and D.K. Lee, *J. Electroceram.* 5, 8 (2002).
31. D.M. Smyth, *J. Electroceram.* 11, 89 (2003).
32. R. Moos and W. Menesklou, *Appl. Phys. A* 61, 389 (1995).
33. R. Moos and K.H. Hardtl, *J. Appl. Phys.* 80, 393 (1996).
34. A.K. Jonscher, *J. Phys. D Appl. Phys.* 32, R57 (1999).
35. L. Fang, F. Xiang, W. Liao, L.J. Liu, H. Zhang, and X.J. Kuang, *Mater. Chem. Phys.* 143, 552 (2014).
36. L.J. Liu, H.Q. Fan, L. Fang, X.L. Chen, H. Dammak, and M.P. Thi, *Mater. Chem. Phys.* 117, 138 (2009).
37. W.S. Lau and T. Han, *Appl. Phys. Lett.* 86, 152107 (2005).
38. S.Y. Zheng, E. Odendo, L.J. Liu, D.P. Shi, Y.M. Huang, L.L. Fan, J. Chen, L. Fang, and B. Elouadi, *J. Appl. Phys.* 113, 094102 (2013).